Planetary and Space Science 113-114 (2015) 347–358

Contents lists available at ScienceDirect

Planetary and Space Science

journal homepage: www.elsevier.com/locate/pss

# Rotational temperatures of Venus upper atmosphere as measured by SOIR on board Venus Express

A. Mahieux [a,b,c,*], A.C. Vandaele [a], S. Robert [a], V. Wilquet [a], R. Drummond [a], M.A. López Valverde [c], M. López Puertas [c], B. Funke [c], J.L. Bertaux [d,e]

[a] Planetary Aeronomy, Belgian Institute for Space Aeronomy, 3 av. Circulaire, 1180 Brussels, Belgium
[b] Fonds National de la Recherche Scientifique, rue d'Egmont 5, B-1000 Brussels, Belgium
[c] Instituto de Astrofísica de Andalucía, CSIC, Glorieta de la Astronomía s/n, 18008 Granada, Spain
[d] LATMOS, 11 Bd d'Alembert, 78280 Guyancourt, France
[e] Institut Pierre Simon Laplace, Université de Versailles-Saint-Quentin, 78280 Guyancourt, France

ARTICLE INFO

*Article history:*
Received 23 February 2014
Received in revised form
19 June 2014
Accepted 4 December 2014
Available online 2 January 2015

*Keywords:*
Planetary atmosphere
Venus
Rotational temperature

ABSTRACT

SOIR is a powerful infrared spectrometer flying on board the Venus Express spacecraft since mid-2006. It sounds the Venus atmosphere above the cloud layer using the solar occultation technique. In the recorded spectra, absorption structures from many species are observed, among them carbon dioxide, the main constituent of the Venus atmosphere. Previously, temperature vertical profiles were derived from the carbon dioxide density retrieved from the SOIR spectra by assuming hydrostatic equilibrium. These profiles show a permanent cold layer at 125 km with temperatures of ~100 K, surrounded by two warmer layers at 90 and 140 km, reaching temperatures of ~200 K and 250–300 K, respectively. In this work, temperature profiles are derived from the SOIR spectra using another technique based on the ro-vibrational structure of carbon dioxide observed in the spectra. The error budget is extensively investigated. Temperature profiles obtained by both techniques are comparable within their respective uncertainties and they confirm the vertical structure previously determined from SOIR spectra.



## 1. Introduction

The Venus terminator is a poorly known region of the Venus atmosphere. Previous measurements of temperature concentrated either on a narrow altitude region (Sonnabend et al., 2012) or on specific locations (Seiff et al., 1980). The SOIR (Solar Occultation in the InfraRed) instrument on board the European Space Agency (ESA) Venus Express (VEx) spacecraft is orbiting Venus since mid-2006 (Titov et al., 2006a, 2006b) and is the first instrument that regularly sounds that region. SOIR is an infrared spectrometer sounding the Venus mesosphere and lower thermosphere (70–160 km) by using the solar occultation technique (Bertaux et al., 2007; Mahieux et al., 2008; Nevejans et al., 2006). The instrument records transmittance spectra in the near-infrared region (2200–4400 $cm^{-1}$) where a large inventory of species have spectral signatures; among them carbon dioxide, the main constituent of the Venus atmosphere (96.5%).

Temperature profiles in the upper atmosphere were previously obtained from the carbon dioxide number density profiles derived from the SOIR spectra by using the hydrostatic equation (Mahieux et al., 2015, 2010, 2012) and assuming the $CO_2$ volume mixing ratio (VMR) from VIRA (Venus International Reference Atmosphere) (Hedin et al., 1983; Zasova et al., 2006). All the temperature profiles systematically show a succession of warm and cold layers. Starting from the bottom, a warm layer is observed at approximately 95 km reaching ~200 K, above which a very cold layer at ~125 km is observed, with temperatures dropping as low as 100 K. A second warmer layer is located at 140 km with temperatures between 250 and 300 K (Mahieux et al., 2015). Such a structure was observed in previous measurements (Seiff et al., 1980) and predicted by model simulations, such as the Venus Thermospheric General Circulation Model (VTGCM) (Bougher, 1995; Bougher et al., 2015). Apparently, it can be explained by $CO_2$ radiative energy deposition and emission at different wavelengths (see Brecht and Bougher, 2012 for a review). However, the amplitude of the variations at these altitudes and at the terminator was not observed before. The lower warmer layer at 90–100 km on the Venus night side has been recently confirmed by the SPICAV-UV/VEx (Piccialli et al., 2015).

In the companion paper (Mahieux et al., 2015), the SOIR hydrostatic temperature profiles are compared with literature profiles from SPICAV-UV/VEx (Mahieux et al., 2015; Piccialli et al., 2015), VeRa/VEx (Piccialli et al., 2012) and ground-based sub-mm measurements from Clancy et al. (2012, 2003); comparison with VIRA

* Corresponding author.
*E-mail address:* arnaud.mahieux@aeronomie.be (A. Mahieux).

http://dx.doi.org/10.1016/j.pss.2014.12.020
0032-0633/

can be found in Mahieux et al. (2012). The comparison with the SOIR hydrostatic temperature profiles shows a good agreement, even if none of the literature profiles were taken at the terminator.

The aim of this paper is to present the rotational temperatures derived from the carbon dioxide rotational structure observed in the SOIR spectra. This is a different and independent technique, and hence we expect to either corroborate or contradict the SOIR temperatures previously derived by using the $CO_2$ number densities and the hydrostatic equilibrium approach. The rotational structure of different $CO_2$ absorption bands is studied to determine the rotational temperature. In the following sections we described the method, the sources of errors and the major features in the data. Finally, the temperatures derived are presented and the results from both techniques are compared.

## 2. Instrument description

The SOIR instrument has been extensively described in previous publications (Mahieux et al., 2008, 2009; Nevejans et al., 2006; Vandaele et al., 2013), and only its main characteristics are reported here.

SOIR operates in the 2.2 to 4.4-μm near-IR region (2200–4400 $cm^{-1}$). It is made of an echelle grating for the light diffraction, used at very high diffraction orders, between 101 and 194 (Nevejans et al., 2006). The spectral region covered by each order can be found in Vandaele et al. (2013). An acousto-optic tunable filter (*AOTF*) is placed right after the instrument entrance optics to select the appropriate wavenumber region, which encompasses the selected diffraction order of the echelle grating. The shape of the transfer function of the *AOTF* is a sinc square-like function, and its full width at half maximum (FWHM, ~24 $cm^{-1}$) is a bit larger than the free spectral range of the echelle grating (~22 $cm^{-1}$). This produces an overlap of adjacent orders in the recorded spectra (Mahieux et al., 2008, 2009), which creates leakage from the adjacent orders on the detector, in such a way that absorption lines from the first adjacent orders are also present in the recorded spectra. Moreover, these lines are modulated by the *AOTF* transfer function.

The spectra are recorded on a detector cooled down to 78 K to decrease the noise level; it is composed of 320 pixel columns in its spectral direction and 32 pixel rows in its spatial direction. The pixel rows in the spatial direction are combined on-board into two bins of data. SOIR has the capability to measure up to four different diffraction orders in a one second sequence. Altogether they are recorded on the two detector bins, and form eight independent spectra (Vandaele et al., 2013). The main instrument characteristics are summarized in Table 1 for a few diffraction orders.

SOIR sounds the Venus atmosphere above the cloud deck, in the 70 to 160 km region, which corresponds to the mesosphere and lower thermosphere, by using the solar occultation technique. Therefore, measurements are always taken either at 6 AM or 6 PM local solar time. Observations cover all latitudes from the North Pole to the South Pole. Due to the eccentricity of the VEx orbit, measurements taken close to the North Pole have a very good vertical resolution (~200 m), while the ones close to the South Pole have a coarser vertical resolution (up to 5 km). The vertical sampling also varies with the latitude: ~2 km close to the North Pole, ~500 m between 40° and 70° North, and up to 5 km close to the South Pole.

**Table 1**
SOIR main instrument characteristics for selected diffraction orders.

| Instrument characteristics | Order 101 | Order 148 | Order 194 |
|---|---|---|---|
| Centre of the order [$cm^{-1}$] | 2266.7 | 3321.5 | 4353.8 |
| Spectral interval on the detector [$cm^{-1}$] | 19.4 | 28.4 | 37.2 |
| Spectral resolution [$cm^{-1}$] | 0.11 | 0.16 | 0.21 |
| Spectral sampling interval [$cm^{-1}$] | 0.061 | 0.089 | 0.117 |
| Typical signal to noise ratio | 1500 | 3000 | 1000 |

The altitude associated to a spectrum corresponds to the tangent altitude at which it was recorded. This altitude is calculated as the minimum distance between the Venus surface and the line of sight that connects the centre of the considered bin and the targeted point on the Sun surface (Vandaele et al., 2013). A series of spectra taken for the same order and bin are measured in a sequence of increasing tangent altitudes for an egress phase (sunrise), and decreasing altitudes in the case of ingress (sunset).

In the IR spectral region of interest, carbon dioxide presents many absorption bands, from various isotopologues and showing large variations in intensity: strong bands in the 2.6 μm region are detected as high as 165 km, while weaker bands at 2.99 μm and 3.98 μm allow measurements as low as 90 km (Mahieux et al., 2015, 2010, 2012).

## 3. The rotational temperature method

We describe here a rapid method to determine the rotational temperature from single transmittance spectra. In this method we

(1) Do not require the knowledge of the $CO_2$ density profile;
(2) Do not require the exact knowledge of the line of sight (LOS) and, in particular, the ray tracing calculation through the different layers of the atmosphere;
(3) Consider that all atmospheric variables at a given tangent altitude are not influenced by their values at the layers above. This is a reasonable approach particularly for temperature since the information contained in the transmittance originates mostly from the temperature at the tangent altitude, and is weakly influenced by the layers above;
(4) Do not require the computationally expensive simulation of spectra including all instrumental effects, in particular the convolution by the instrument spectral function. The instrumental effects are directly accounted for in the rotational temperature calculation.

Nevertheless, in the following sections we estimate the impact of these assumptions on the retrieved temperature.

### 3.1. The method

The ro-vibrational spectral structure of the $CO_2$ absorption bands is used to calculate the rotational temperature. SOIR is capable of resolving the lines in the $CO_2$ P- and R-branches, although not those in the Q-branch. The strength of the ro-vibrational lines is given by (e.g., see Herzberg, 1950):

$$I_{ij} = \frac{C_{abs} \times \nu_{ij}}{Q_r(T)} \times e^{-E_i(hc/kT)} \left(1 - e^{-\nu_{ij}(hc/kT)}\right) \times S_{ij} \times F \quad (1)$$

where $T$ is the temperature [K], $i$ and $j$ are the lower and upper rotational levels, $I_{ij}$ is the intensity of the absorption line [$cm^{-1}$/(molecules $cm^{-2}$)], $C_{abs}$ represents constants for the transition, $\nu_{ij}$ is the line position [$cm^{-1}$], $Q_r(T)$ is the rotational partition function, $E_i$ is the lower-state energy [$cm^{-1}$], $S_{ij}$ is the Höln–London factor and $F$ is the Herman–Wallis factor. For the SOIR spectral region and the typical temperatures of the Venus upper atmosphere (100–300 K), the $\left(1 - e^{-\nu_{ij}(hc/kT)}\right)$ factor can be assumed equal to 1 within a high precision.

Line parameters are taken from the HITRAN spectroscopic database (Rothman et al., 2013). The HITRAN notation $v_1 v_2^{l_2} v_3(r)$ is adopted here for the vibrational state assignment of $CO_2$ (Rothman

et al., 2005): $v_j$ represents the quantum number associated with the normal mode of vibration $j$, $l_j$ is the vibrational angular momentum quantum number associated with the degenerate bending mode $j$, and $r$ is the unity for the highest vibrational level of a Fermi resonance group (Rothman and Young, 1981).

The Höln–London factor in Eq. (1) is calculated following the relation obtained from Amyay (2012). The Herman–Wallis factors are polynomials having the form:

$$F = 1 + a_1 m + a_2 m^2 + a_3 m^3 \quad (2)$$

with $m$ equals to $J+1$ for a R-branch and $-J$ for a P-branch, and $a_1$, $a_2, a_3$ are tabulated coefficients for a given vibrational transition and are obtained from Johns and Vander Auwera (1990), Malathy Devi et al. (1998), Toth et al. (2007) (see Table 2), since they are not tabulated in the HITRAN database.

The absorption bands used here to determine the rotational temperature are listed in Table 2. For each of them, we have indicated the isotopologue involved, the SOIR diffraction orders and spectral regions as well as the approximate altitude region (Mahieux et al., 2010, 2012) in which the band is used. The rotational lines observed and the Herman–Wallis coefficients are also indicated. The labelling of the band follows the notation defined in HITRAN: $v_1 v_2^{l_2} v_3(r)$ (Rothman et al., 2005).

Eq. (1) can be re-written as a linear expression of the line intensity as a function of the energy of the lower rotational level by

$$\frac{\log(I_{ij}/\nu_{ij} S_{ij} F)}{(hc/k)} = -\frac{E_i}{T} + C \quad (3)$$

where $C$ is a constant for a given vibrational band. The temperature is obtained as the inverse of the first order coefficient of the linear fit. In the linear regression, a weight inversely proportional to the error bar is associated to each point. The error on the rotational temperature is obtained from the uncertainty from the linear fit weighted by the uncertainties on the line intensities which is derived from the noise in the measured spectra, taken as the square root of the covariance of this linear regression.

All the bands included in this study are fundamental transitions, i.e. the lower vibrational state is the ground state of the molecule. The hot bands of $CO_2$ in the SOIR wavenumber range all present too weak signal. The absence of these bands impedes studying vibrational non-local thermodynamic equilibrium (non-LTE) in the $CO_2$ states. To correctly retrieve the temperature using Eq. (3), lines with $J''$ smaller than 10 and higher than 36 are not considered because they are very noisy.

The transmittance $\tau$ is calculated from the lines intensity values $I_{ij}$ using the Beer–Lambert law (Herzberg, 1950):

$$\tau = \exp(-n \cdot s \times I_{ij}) \quad (4)$$

where the $n \cdot s$ product is the integrated column density along the line of sight, or slant density. We adopted a Voigt line shape whose intensity is given by $I_{ij}$ from Eq. (1) and whose width depends on the pressure and the temperature through the Doppler and Lorentzian widths calculated at the temperature and pressure of the considered layer. To retrieve the line intensity from a transmittance spectrum, Eq. (4) is used and the line shape is fitted using the SOIR instrument line shape (ILS) which is given by a Gaussian with a FWHM corresponding to the instrument spectral resolution (Vandaele et al., 2013). Hence, all lines are convolved by a Gaussian of width varying between 0.11 and 0.21 $cm^{-1}$, depending on the order (see Table 1). Saturated lines are avoided in the retrieval since they do not contain information of the atmosphere at the tangent height.

The validity and precision of Eq. (3) have been tested on the $20^00(3)$–$00^00(1)$ transition of $^{16}O^{12}C^{18}O$, simulated at a temperature of 200 K and considering a total pressure of 0.01 mbar and an integrated density of $10^{20}$ molecules $cm^{-2}$. The synthetic transmittance of the band in this idealized case is presented in Fig. 1 (panel 1), with the rotational assignment of each line, and the fit is plotted in panel 2. The $I_{ij}$ values are directly taken from HITRAN (Rothman et al., 2013), and their errors have been taken from the HITRAN database. The fit is calculated in this particular case on 48 points, corresponding to the 48 selected absorption lines. The fitted temperature is $197.9 \pm 2.8$ K. The difference to the simulated temperature is equal to 2.1 K or 1.05 %. One could have expected a fitted temperature of exactly 200 K, since the temperature has been retrieved from an ideal synthetic spectrum, with no added noise. However, we have considered the errors of the spectroscopic coefficients as given in the HITRAN database, with values between 10 and 20% for the band simulated here are all measured values (Rothman et al., 2013). Also, the Herman–Wallis coefficients are calculated values with a relatively low precision (between 2 and 4 precision digits).

In the following sections, we investigate the impact of several errors sources on the retrieved temperature. These include: layering of the atmosphere, and instruments factors like the *AOTF* transfer function modulation, the order addition, the instrument line shape and the instrumental noise.

### 3.2. Error induced by not considering atmosphere layering

In Eq. (3), the layering of the atmosphere is not introduced, in order to remain independent from the SOIR retrieved $CO_2$ number density profile. However, in reality, the transmittance spectrum taken at a given tangent height has a contribution (in terms of absorption) from the atmospheric layer at that tangent height and also from the layers above (see Fig. 2). As we neglect the contributions of the layers above, we need to evaluate the impact of such an approximation on the retrieved rotational temperature.

We consider here that the layer thickness, or the altitude difference between two successive tangent points, is constant during an

**Table 2**
List of the bands and ro-vibrational transitions used to determine the rotational temperature in the 16 considered wavenumber regions (orders).

| Vibrational transition | Isotopologue | SOIR diffraction orders | Spectral region [$cm^{-1}$] | Observed rotational transitions $J$ | Herman–Wallis coefficients | | | Altitude region [km] |
|---|---|---|---|---|---|---|---|---|
| | | | | | $a_1$ ($10^{-4}$) | $a_2$ ($10^{-5}$) | $a_3$($10^{-6}$) | |
| $20^00(3)$–$00^00(1)$ | $^{16}O^{12}C^{18}O$ | 111–112 | 2481–2524 | P27e–R30e | −0.569[a] | 3.362[a] | – | 120–90 |
| $21^10(3)$–$00^00(1)$ | $^{12}C^{16}O_2$ | 141–142–143 | 3151–3223 | P40e–R50e | 4711[b] | 0[b] | 14.6 [b] | 120–90 |
| $21^10(2)$–$00^00(1)$ | $^{12}C^{16}O_2$ | 148–149–150 | 3307–3381 | P40e–R52e | 1609[b] | −1.8[b] | 1.56[b] | 130–90 |
| $10^01(2)$–$00^00(1)$ | $^{13}C^{16}O_2$ | 156–157–158 | 3486–3561 | P46e–R48e | −90[c] | 2.1[c] | – | 140–120 |
| $10^01(2)$–$00^00(1)$ | $^{12}C^{16}O_2$ | 160–161–162 | 3576–3652 | P40e–R64e | 100[b] | 1.57[b] | – | 140–120 |
| $10^01(1)$–$00^00(1)$ | $^{12}C^{16}O_2$ | 164–165–166 | 3665–3742 | P52e–R40e | −160[b] | −0.684[b] | – | 160–130 |

[a] Toth et al. (2007).
[b] Malathy Devi et al. (1998).
[c] Johns and Vander Auwera (1990).

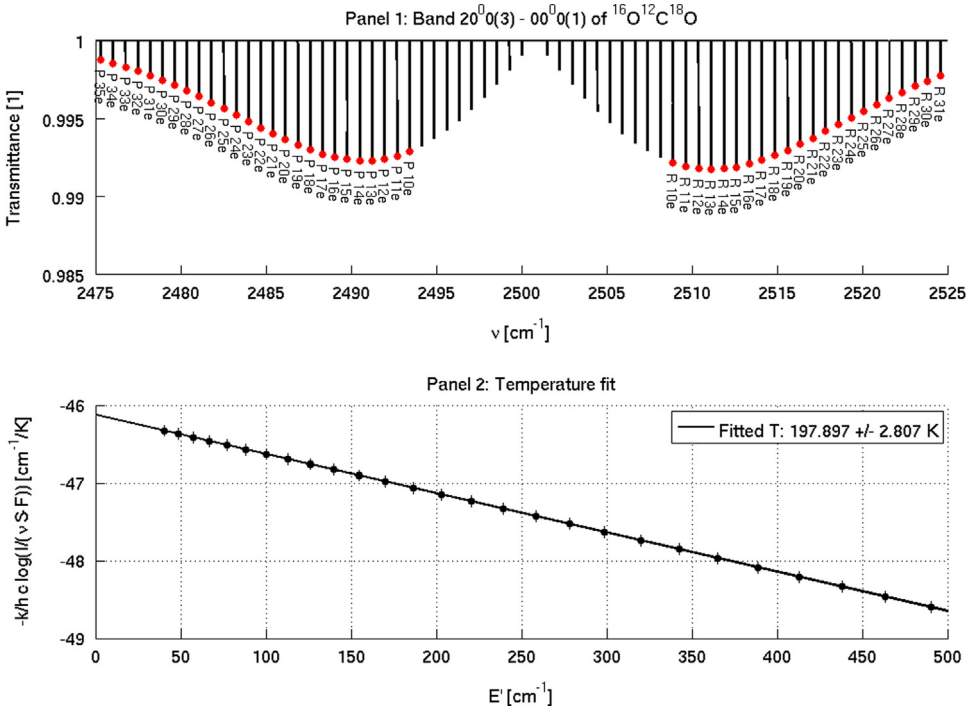


**Fig. 1.** Fit of the rotational temperature (using Eq. (3)) from a synthetic transmittance for the $20^00(3)$–$00^00(1)$ transition of $^{16}O^{12}C^{18}O$. Upper panel, the simulated spectrum with the assigned rotational transitions. Lower panel, the linear fit corresponding to the retrieved rotational temperature of $197.9 \pm 2.8$ K.

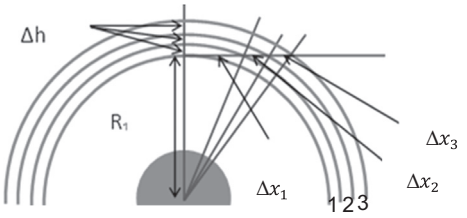


**Fig. 2.** Geometry of the limb sounding (e.g., Eq. (5) for $j$ equals 3). $R_1$ is the altitude of the innermost layer, $\Delta h$ is the layer thickness, $\Delta x_1$, $\Delta x_2$ and $\Delta x_3$ are the path lengths in the respective layers 1, 2 and 3.

occultation. The SOIR altitude measurement shows mean variations of the layer thickness of the order of 3% during an occultation, which is considered as negligible here. If $i$ layers of constant thickness $\Delta h$ are considered, it is possible to estimate the ratio of the integrated density in the innermost layer 1 to the integrated density in the layer $j$ (see Fig. 2), assuming that the total pressure profiles follows an exponential law:

$$\begin{cases} \Delta x_1 = \sqrt{(R_1+\Delta h)^2 - R_1^2} \\ \sum_{i=1}^{j} \Delta x_i = \sqrt{(R_1 + j\,\Delta h)^2 - R_1^2} \Rightarrow \dfrac{\Delta x_1\, n_1}{\sum_{i=1}^{j} \Delta x_i\, n_i} \approx \dfrac{1}{\sqrt{j}} \exp\left(\dfrac{(j-1)\Delta h}{H}\right) \\ p_j = p_1 \exp\left(-\frac{(j-1)\Delta h}{H}\right) \end{cases} \tag{5}$$

where $R_1$ is the distance between the centre of Venus and the tangent point in layer 1, $H$ is the $CO_2$ scale height (approx. 3–8 km in the SOIR measurement altitude region) and $p$ is the total pressure. The different geometrical quantities are showed in Fig. 2. In these equations, simplifications are made considering the following facts. First, the distance from the tangent point to the centre of Venus is much larger than the altitude difference between two successive layers ($R_1 \gg \Delta h$). Second, the temperature profile is constant enough so that we can write $p_j = p_1 \times \exp(-((j-1) \times \Delta h)/H)) \Rightarrow n_j = n_1 \times \exp(-((j-1) \times \Delta h)/H))$ without introducing a significant error; $n$ being the total density.

As an example, for a layer thickness of 0.5 km typical for SOIR Northern Hemisphere measurements, and considering $j=3$, the ratio is equal to 0.741, meaning that 74.1% of the transmittance originates from the innermost layer.

In order to check the validity of this approximation, a series of synthetic spectra have been calculated, accounting for the atmospheric layering, simulating the $20^00(3)$–$00^00(1)$ transition of isotopologue $^{16}O^{12}C^{18}O$. The imposed temperature profile is presented as the dashed profile in the left Panel of Fig. 3. The number density profile is a typical Venus $CO_2$ density profile, varying exponentially between $6.5 \times 10^9$ molecules $cm^{-3}$ at 140 km and $10.5 \times 10^{14}$ molecules $cm^{-3}$ at 100 km. It is taken from the VAST data compilation (Venus Atmosphere from SOIR measurements at the Terminator (Mahieux et al., 2015, 2012)). Eq. (3) is applied without any correction on each transmittance of the solar occultation series. The line intensities are directly taken from HITRAN, and the error as the uncertainty reported in the same database. The retrieved temperature profile is given as the solid profile in the same panel. The difference between the two profiles in percent is given in the right panel of the same Figure. The values of the uncertainties vary between 5 K and 30 K above 110 km and up to 140 K at 100 km. Between 142 km and 107 km, the maximum retrieval difference with the a-priori temperature profile due to the layering is less than 15 K, or 9.4%. Below 107 km, there is a clear divergence between the two profiles: the atmospheric absorption lines become saturated, and Eq. (3) is no longer valid.

Since we want to remain independent from the $CO_2$ number density profile in the rotational temperature profile derivation, the atmospheric layering induced by the solar occultation measurement technique will not be considered here. Hence, considering the layering would imply the concurrent retrieval of the $CO_2$ number density, see Eq. (7) from Mahieux et al. (2012). As a consequence, the above-described calculation shows that the systematic error in the rotational temperature introduced by the retrieval is lower than 15 K.

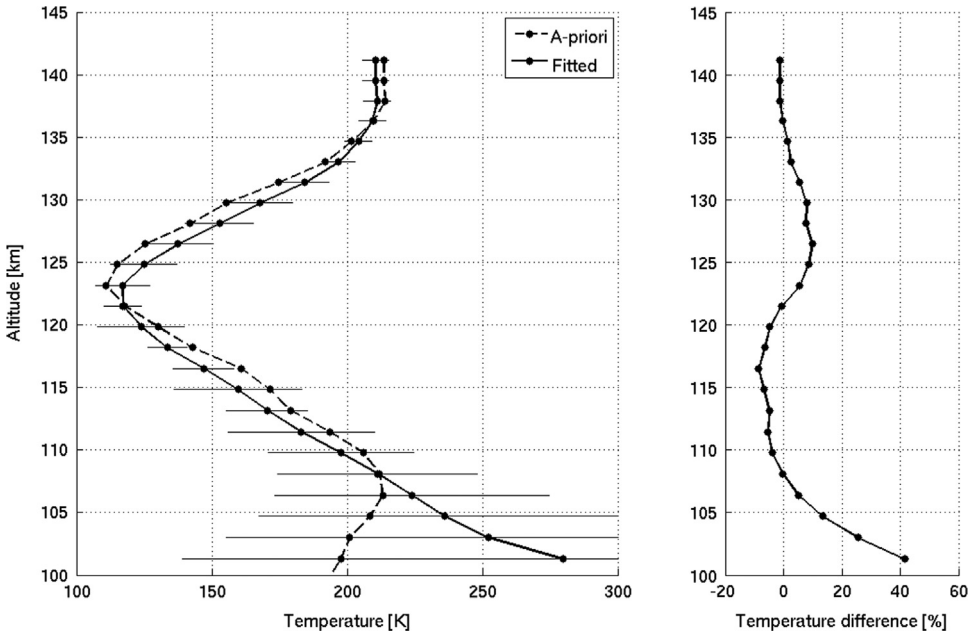


**Fig. 3.** Fit of the rotational temperature of the $20^{0}0(3)$–$00^{0}0(1)$ band of $^{16}O^{12}C^{18}O$ in the 100 to 142 km region. Left panel: the dashed temperature profile is the a-priori profile, used to build the synthetic spectra; the temperature profile in solid line is the retrieved temperature distribution, together with its uncertainty. Right panel: difference between a-priori and retrieved temperature profiles, in percent.

### 3.3. Error induced by not considering the AOTF transfer function and the order addition

When light enters the SOIR instrument it is modulated by the *AOTF* transfer function. Because the bandpass of this filter is larger than the free spectral range of the echelle grating, overlapping of adjacent orders occurs on the detector. The equation to construct a synthetic spectrum taking into account this overlap is given by Mahieux (2011):

$$Tr_L = \frac{\sum_{p=-n_{orders}}^{n_{orders}} BF \times AOTF_p \times R_S \times I_{atm}}{\sum_{p=-n_{orders}}^{n_{orders}} BF \times AOTF_p \times R_S} \quad (6)$$

where $Tr_L$ is the transmittance spectrum of layer $L$, $n_{orders}$ is the number of adjacent orders considered on each side of the central order, $BF$ is the grating Blaze function, $AOTF_p$ is the *AOTF* transfer function value in order $p$, $R_S$ is the solar radiance spectrum and $I_{atm}$ is the atmospheric spectrum. Consideration of up to three orders below and above the order under study is usually sufficient for the calculation of the SOIR synthetic spectra.

In the present study, however, where we derive the rotational temperature, only the lines coming from the central order are considered. The uncertainty of the *AOTF* transfer function becomes larger in the adjacent orders, and this introduces a large uncertainty on measurement of the depth of the absorption lines. But the modulation of the observed spectrum by the *AOTF* transfer function needs to be considered, see Eq. (6). To better measure the line absorption depths, the spectrum is divided by the value of the SOIR central order bandpass $AOTF_0$ and the contribution of the adjacent orders' bandpass is subtracted to obtain the corrected spectrum $Tr_{corr,L}$:

$$Tr_{corr,\,L} = \frac{Tr_L \sum_{p=-n_{orders}}^{n_{orders}} AOTF_p - \sum_{p=-n_{orders}}^{-1} AOTF_p - \sum_{p=1}^{n_{orders}} AOTF_p}{AOTF_0} \quad (7)$$

To validate this procedure, a synthetic spectrum is built considering the correct *AOTF* function and order addition; no atmospheric layering is considered here. It is tested on the $20^{0}0(3)$–$00^{0}0(1)$ transition of $^{16}O^{12}C^{18}O$, calculated at a temperature of 200 K. The calculated synthetic transmittance of the band is presented Fig. 4 (upper panel), considering three adjacent orders on each side of the main one (central order 112 is considered here). The rotational assignments corresponding to each line are also indicated. In this figure, weaker lines appear between the stronger ones that correspond to the adjacent orders (in this case mainly from orders 111 and 113), modulated by the *AOTF* transfer function. The lines considered in the linear fit are also shown. Only lines with $J''$ larger than 10 and lower than 36 are considered. Their intensities are measured calculating the area under each line, using an area integration function. In the lower panel we present the linear fit and the fitted temperature of $202.9 \pm 5.7$ K. This differs from the a-priori temperature by 2.9 K or 1.45%. We used 16 absorption lines in this fit.

### 3.4. Measurement of the depth of the absorption lines

The instrumental resolution also needs to be taken into account to correctly simulate the spectra. By slightly modifying Eq. (6), we get (Mahieux, 2011)

$$Tr_{conv,L} = \frac{\sum_{p=-n_{orders}}^{n_{orders}} BF \times AOTF_p[(I_S \times I_{atm}) \otimes G(\sigma)]}{\sum_{p=-n_{orders}}^{n_{orders}} BF \times AOTF_p[I_S \otimes G(\sigma)]} \quad (8)$$

where $\otimes$ denotes the convolution product, $G(\sigma)$ is the Gaussian ILS and $\sigma$ is the instrument resolution. To retrieve absorption lines spectroscopic characteristics from the SOIR spectra, a fit to a Gaussian function is used, returning the position of the line, its absorption depth and FWHM, and the errors of each of these parameters. Only lines with a measured FWHM within 10% of the SOIR resolution are considered, and that are located within 1 detector pixel (see Table 1 for approximate wavenumber value) relative to their centre wavenumber as listed in HITRAN. These constrains ensure that only well resolved isolated lines are considered, and thus removing the effects of potential contributions of lines from the same or adjacent orders.

A sufficient number of lines should be considered to accurately retrieve the temperature through the linear fit process, and also ensure that they are sufficiently separated in wavenumber, i.e. with large $J''$ differences. In the present study, a minimum value of

4 lines is chosen, imposing a minimum $J''$ difference between lines of 10.

The effect of the convolution on the retrieved rotational temperature is also tested. This is performed by building a synthetic transmittance spectrum considering only the convolution of the spectrum by the SOIR ILS. The results are presented in Fig. 5 for the $20^00(3)$–$00^00(1)$ transition of $^{16}O^{12}C^{18}O$, calculated at a temperature of 200 K. Here we used 33 lines assuming Gaussians line shapes. The SOIR spectral resolution at these wavenumbers is 0.12 $cm^{-1}$. The line intensities are directly measured on the synthetic spectrum using the Gaussians, and the error coming from the fit is used as weighting factors. The retrieved temperature is $198.1 \pm 2.5$ K. The uncertainty on the temperature retrieval is small because all the absorption lines are well separated (there is no instrumental order addition, and only one band is considered here).

### 3.5. Calculation of the error on the temperature

To evaluate the error on the retrieved temperature random noise is added to the synthetic spectra corresponding to typical noise measured in the SOIR spectra, equivalent to a signal to noise ratios (SNR) of 1000, 2000 and 3000. These calculations have been performed for on the $20^00(3)$–$00^00(1)$ transition of $^{16}O^{12}C^{18}O$.

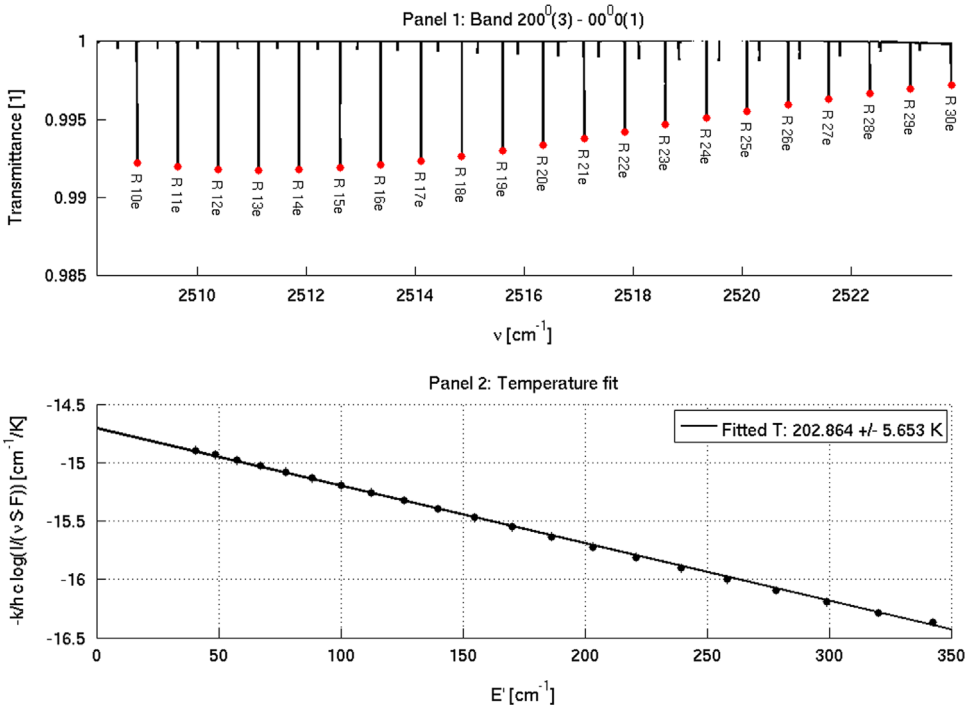


**Fig. 4.** Error induced in the rotational temperature by not considering the *AOTF* transfer function and the order addition for the transition $2000(3)$–$00^00(1)$ band of $^{16}O^{12}C^{18}O$ at a tangent altitude of 118.2 km. Upper panel: the simulated spectrum with the assignment of the rotational transitions. Lower panel: the linear fit together with the retrieved temperature and its error.

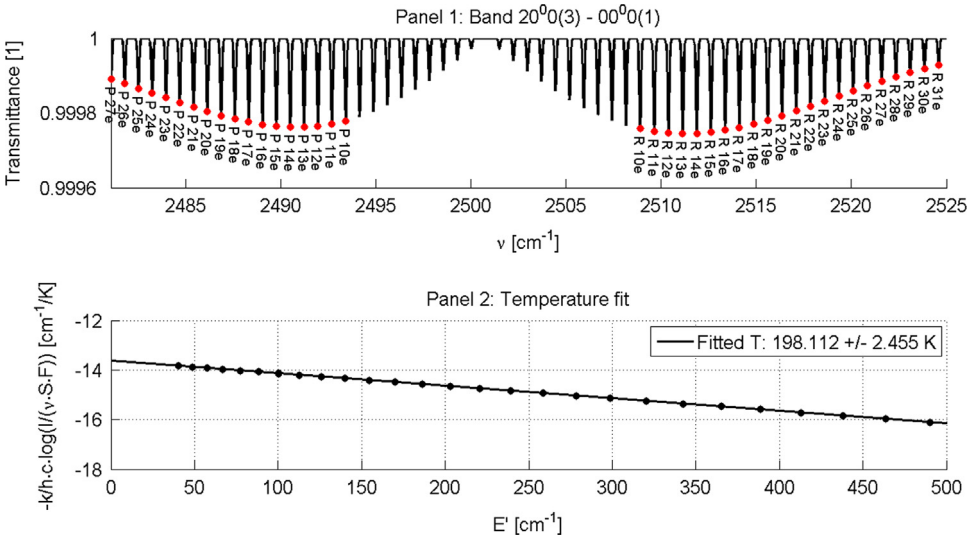


**Fig. 5.** Error induced in the rotational temperature by some approximations (see text) considering the SOIR instrument line profile to calculate the synthetic spectrum for the transition $20^00(3)$–$00^00(1)$ band of $^{16}O^{12}C^{18}O$ at a temperature of 200 K. Upper panel, the spectrum with the assignment of the rotational transitions. Lower panel, the linear fit obtained when retrieving the line intensities using a Gaussian function and the retrieved temperature and its error.

The rotational temperature retrievals are presented in Fig. 6 for SNR of 1000, 2000 and 3000 respectively, typical for SOIR measurements (see Table 1). The right panel presents the difference between the retrieved profiles and the a-priori temperature profile. The fit is performed in the 100 to 118 km region. At higher altitudes, the absorption signature is below the noise level and, below 105 km, the absorption lines are saturated. As expected, the fit gets better with higher SNR and the uncertainties on the retrieved profile are smaller. For the larger SNR the retrieved temperatures differ in less than 25% from the a-priori temperature.

### 3.6. Summary of the error sources

To summarize, the main source of error comes from the spectral noise, followed by the non-consideration of the contribution of the layers above the main tangent height and the instrument characteristics (*AOTF*, order addition and SOIR spectral resolution). The total (combined from all error sources) error expected in the retrieval of the rotational temperature on the SOIR database ranges from 20 to 200 K, depending on the value of the SNR. The difference between the retrieved temperature profiles and the temperature profiles used to build the synthetic spectra vary between 10 and 50 K, thus lower than the expected total errors.

## 4. Results and discussion

The technique described above has been applied on a subset of orbits during which $CO_2$ was observed from very high altitudes in the thermosphere (165 km) down to the mesosphere at 70 km. 125 orbits were selected, with 548 spectral datasets, and are presented in Table 3. The rotational temperature profiles that were showing very large uncertainties on the whole profile (all larger than 100 K), and for which the rotational temperature profile is in total disagreement (no rotational temperature within the hydrostatic temperature profile uncertainty) with the hydrostatic profile have been discarded. This concerns 80 profiles over the 548 individual rotational temperature profiles, or 14.6%. These profiles are not displayed in the current analysis.

The retrieved rotational temperature profiles are presented in Fig. 7 for the six selected orbits marked with a star in Table 3.

In each panel, the hydrostatic temperatures are presented, together with their uncertainties. The rotational temperature profiles are also plotted together with their estimated error. Although the uncertainties are very large, varying between 10 and 80 K for the hydrostatic temperature, and between 10 and 150 K for the rotational temperature, the systematic overlap of the profiles, within their uncertainties, shows a reasonable agreement. The rotational temperatures are retrieved only when the criteria specified in Section 3 are satisfied, i.e., no saturation in the lines of the band, isolated lines, and large enough number of lines to calculate the linear fit. For this reason, the retrieved temperatures are not uniformly distributed in altitude and there are some gaps with few or no temperatures (see Fig. 8).

For some profiles, the large variations observed at adjacent altitudes are caused by the large spectral noise error. Remembering that the temperature at a given altitude is derived independently of the surrounding levels (see Section 3 paragraph b), we see that the errors of the rotational temperatures are larger than those of the hydrostatic temperatures.

Unfortunately, only a small number of spectra are available in the cold layer region (120–130 km). At these altitudes, the strong bands that absorb in the 3570–3740 $cm^{-1}$ region are saturated, while the weaker bands from the 2500, 2600 and 3100–3380 $cm^{-1}$ regions present absorption structures below the noise level. The only available band is the $10^01(2)–00^00(1)$ transition of $^{13}C^{16}O_2$ at 3500 $cm^{-1}$. But the spectra measured in this order (156) are contaminated by lines coming from adjacent orders of the much stronger band at 3570 $cm^{-1}$ ($10^01(2)–00^00(1)$ transition of $^{12}C^{16}O_2$), which often prevents from retrieving the rotational temperature with the method described above.

A statistical study has been performed on the dataset focusing on the agreement between the hydrostatic and rotational temperature results, considering (i) the complete available profile; (ii) the top warm layer at 150 km; (iii) the cold layer at 125 km; and (iv) the bottom warm layer at 100 km.

(i) 76% of the rotational temperature profiles show a good agreement (within the $1-\sigma$ uncertainty) with the hydrostatic temperature profiles;
(ii) 79% of the profiles obtained with the rotational method have data at the altitude of the top warm layer (150 km), of which 88% are in agreement with and confirm the hydrostatic results;
(iii) For the cold layer (125 km), the respective numbers are 28% and 95%;
(iv) And finally, for the bottom warm layer (100 km), the numbers are 69% and 73%.

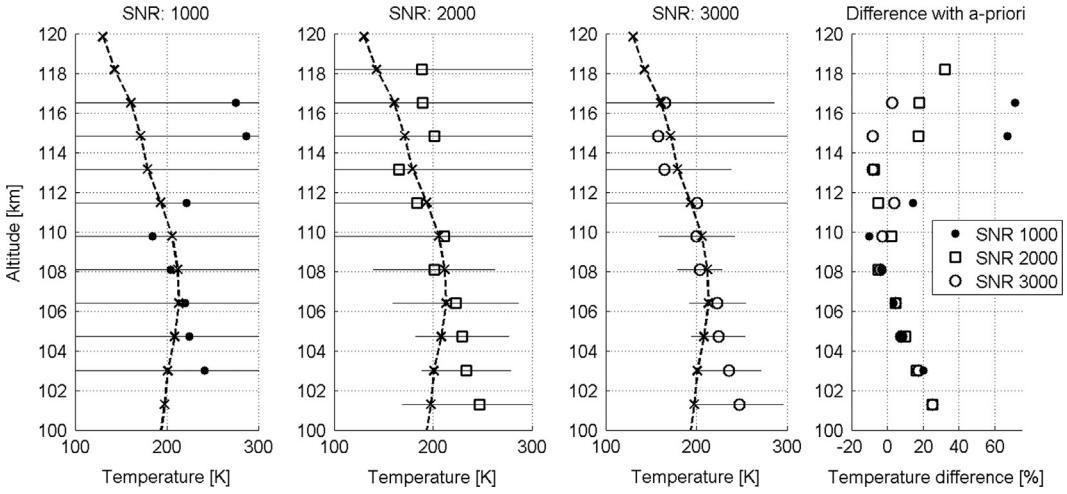


**Fig. 6.** Fit of the rotational temperature of the $20^00(3)–00^00(1)$ of $^{16}O^{12}C^{18}O$ isotopologue in the 100 to 118 km altitude region. Left panels (for SNR of 1000, 2000 and 3000): the dashed lines are the a-priori temperature profile is the a-priori profile, used to build the synthetic spectra, considering all instrument characteristics; dots (SNR 1000), squares (SNR 2000) and circles (SNR 3000) are the retrieved profiles. The horizontal lines are the uncertainties on the temperature. Right panel: difference in percent between the a-priori and the three retrieved temperature profiles.

**Table 3**
List of the orbits considered in this work. The orbits marked by a star are presented in more details in the text, see Fig. 7.

| Orbit number | Date [DD/MM/YYYY] | LST [h] | Lat [deg] | Lon [deg] | Orders | | | |
|---|---|---|---|---|---|---|---|---|
| 35.1 | 6 | 304 | 74 | 26/05/06 | 166 | | | |
| 335.1 | 18 | 319 | −16 | 22/03/07 | 112 | 149 | 166 | |
| 361.1 | 6 | 208 | 79 | 17/04/07 | 112 | 149 | 166 | |
| *593.1 | 6 | 215 | 3 | 12/05/07 | 112 | 149 | 162 | |
| 597.1 | 6 | 226 | 37 | 12/09/07 | 111 | 149 | 161 | |
| 597.2 | 6 | 223 | 59 | 12/09/07 | 111 | 149 | 161 | |
| 667.1 | 18 | 259 | 78 | 17/02/08 | 112 | 149 | 166 | |
| 669.1 | 18 | 263 | 79 | 19/02/08 | 112 | 149 | 166 | |
| 671.1 | 18 | 268 | 81 | 21/02/08 | 112 | 149 | 166 | |
| *674.1 | 18 | 273 | 83 | 24/02/08 | 112 | 149 | 166 | |
| 675.1 | 18 | 275 | 83 | 25/02/08 | 112 | 149 | 166 | |
| 677.1 | 18 | 277 | 84 | 27/02/08 | 112 | 149 | 166 | |
| 679.1 | 18 | 277 | 85 | 29/02/08 | 112 | 149 | 166 | |
| 681.1 | 18 | 274 | 86 | 03/02/08 | 112 | 149 | 166 | |
| *684.1 | 18 | 257 | 88 | 03/05/08 | 112 | 149 | 166 | |
| 685.1 | 18 | 247 | 88 | 03/06/08 | 112 | 149 | 166 | |
| 686.1 | 18 | 235 | 88 | 03/07/08 | 112 | 149 | 166 | |
| 687.1 | 6 | 223 | 88 | 03/08/08 | 112 | 149 | 166 | |
| 688.1 | 6 | 213 | 87 | 03/09/08 | 112 | 149 | 166 | |
| 689.1 | 6 | 205 | 87 | 03/10/08 | 149 | 166 | | |
| 690.1 | 6 | 200 | 87 | 03/11/08 | 149 | 166 | | |
| 691.1 | 6 | 197 | 86 | 03/12/08 | 149 | 166 | | |
| 693.1 | 6 | 194 | 85 | 14/03/08 | 149 | 166 | | |
| 695.1 | 6 | 194 | 84 | 16/03/08 | 149 | 166 | | |
| 697.1 | 6 | 196 | 82 | 18/03/08 | 149 | 166 | | |
| 699.1 | 6 | 198 | 81 | 20/03/08 | 149 | 166 | | |
| 703.1 | 6 | 206 | 77 | 24/03/08 | 112 | 149 | 166 | |
| 705.1 | 6 | 210 | 74 | 26/03/08 | 149 | 166 | | |
| 706.1 | 6 | 212 | 73 | 27/03/08 | 149 | 166 | | |
| 709.1 | 6 | 219 | 67 | 30/03/08 | 112 | 149 | 166 | |
| 710.1 | 6 | 221 | 63 | 31/03/08 | 149 | 166 | | |
| 710.2 | 6 | 217 | 21 | 31/03/08 | 149 | 166 | | |
| 711.1 | 6 | 223 | 58 | 04/01/08 | 149 | 166 | | |
| 711.2 | 6 | 220 | 30 | 04/01/08 | 149 | 166 | | |
| 1121.1 | 18 | 214 | 81 | 16/05/09 | 161 | 162 | | |
| 1124.1 | 18 | 234 | −44 | 19/05/09 | 149 | 166 | | |
| 1126.1 | 18 | 240 | −52 | 21/05/09 | 149 | 166 | | |
| 1128.1 | 18 | 247 | −60 | 23/05/09 | 149 | 161 | 162 | 166 |
| 1130.1 | 18 | 255 | −69 | 25/05/09 | 149 | 166 | | |
| 1132.1 | 18 | 264 | −77 | 27/05/09 | 149 | 166 | | |
| 1137.1 | 6 | 161 | 88 | 06/01/09 | 160 | 164 | 165 | |
| 1139.1 | 6 | 91 | −75 | 06/03/09 | 149 | 166 | | |
| 1141.1 | 6 | 100 | −67 | 06/05/09 | 149 | 166 | | |
| 1154.1 | 6 | 144 | −7 | 18/06/09 | 149 | 161 | 162 | 166 |
| 1252.1 | 6 | 95 | −73 | 24/09/09 | 149 | 164 | 165 | 166 |
| 1254.1 | 6 | 98 | −65 | 26/09/09 | 149 | 166 | | |
| 1256.1 | 6 | 103 | −57 | 28/09/09 | 149 | 166 | | |
| 1258.1 | 6 | 108 | −48 | 30/09/09 | 149 | 166 | | |
| 1381.2 | 6 | 126 | 16 | 31/01/10 | 149 | 165 | 160 | |
| 1461.1 | 18 | 203 | 84 | 21/04/10 | 148 | 160 | 165 | |
| 1462.1 | 18 | 192 | −47 | 22/04/10 | 148 | 156 | 166 | |
| *1464.1 | 18 | 219 | 86 | 24/04/10 | 111 | 150 | 160 | 165 |
| 1465.1 | 18 | 200 | −60 | 25/04/10 | 111 | 149 | 160 | 166 |
| *1467.1 | 18 | 242 | 87 | 27/04/10 | 149 | 150 | 156 | 166 |
| 1469.1 | 18 | 207 | −76 | 29/04/10 | 112 | 148 | 156 | 166 |
| 1480.1 | 6 | 37 | 86 | 05/10/10 | 141 | 150 | 156 | 165 |
| 1565.1 | 18 | 150 | 72 | 08/03/10 | 148 | 165 | | |
| 1567.1 | 18 | 159 | −10 | 08/05/10 | 141 | 149 | 156 | 166 |
| 1581.1 | 18 | 159 | 87 | 19/08/10 | 148 | 165 | | |
| 1697.1 | 18 | 117 | −88 | 13/12/10 | 157 | | | |
| 1789.1 | 18 | 123 | 11 | 15/03/11 | 141 | 156 | | |
| 1798.1 | 18 | 141 | 81 | 24/03/11 | 141 | 156 | | |
| 1804.1 | 18 | 144 | 85 | 30/03/11 | 141 | 156 | | |
| 1807.1 | 18 | 191 | −82 | 04/02/11 | 161 | | | |
| 1895.1 | 18 | 89 | 34 | 29/06/11 | 141 | 149 | 156 | |
| 1895.2 | 18 | 89 | 65 | 29/06/11 | 141 | 149 | 156 | |
| 1902.1 | 18 | 114 | 79 | 07/06/11 | 141 | 150 | 156 | |
| 1904.1 | 18 | 122 | 81 | 07/08/11 | 142 | 149 | 156 | |
| 1910.1 | 18 | 148 | 85 | 14/07/11 | 141 | 148 | 156 | |
| 1914.1 | 18 | 173 | 87 | 18/07/11 | 141 | 150 | 156 | |
| 2153.1 | 6 | 303 | 87 | 13/03/12 | 148 | 156 | 165 | |
| 2159.1 | 6 | 335 | 85 | 19/03/12 | 111 | 149 | 156 | 166 |
| 2238.1 | 18 | 67 | 43 | 06/06/12 | 149 | 156 | 165 | |
| 2238.2 | 18 | 67 | 36 | 06/06/12 | 149 | 156 | 165 | |
| 2254.1 | 18 | 122 | −71 | 22/06/12 | 111 | 156 | | |

**Table 3** (*continued*)

| Orbit number | Date [DD/MM/YYYY] | LST [h] | Lat [deg] | Lon [deg] | Orders | | | |
|---|---|---|---|---|---|---|---|---|
| 2272.1 | 6 | 351 | −18 | 07/10/12 | 150 | 156 | 165 | 165 |
| *2273.1 | 6 | 355 | −11 | 07/11/12 | 111 | 148 | 160 | 166 |
| 2274.1 | 6 | 358 | −4 | 07/12/12 | 150 | 156 | 165 | |
| 2275.1 | 6 | 1 | 3 | 13/07/12 | 149 | 160 | 166 | |
| 2276.1 | 6 | 5 | 12 | 14/07/12 | 111 | 149 | 162 | |
| 2343.1 | 18 | 30 | 32 | 19/09/12 | 149 | 156 | 166 | |
| 2353.1 | 18 | 60 | −23 | 29/09/12 | 142 | 156 | 165 | |
| 2355.1 | 18 | 66 | −31 | 10/01/12 | 150 | 156 | 162 | |
| 2357.1 | 18 | 72 | −39 | 10/03/12 | 143 | 156 | 162 | |
| 2359.1 | 18 | 78 | −47 | 10/05/12 | 149 | 156 | 161 | |
| 2361.1 | 18 | 83 | −55 | 10/07/12 | 148 | 156 | 161 | |
| 2362.1 | 18 | 108 | 86 | 10/08/12 | 141 | 156 | | |
| 2363.1 | 18 | 88 | −62 | 10/09/12 | 149 | 156 | | |
| 2366.1 | 18 | 141 | 88 | 10/12/12 | 149 | 156 | 160 | |
| 2368.1 | 18 | 166 | 88 | 14/10/12 | 143 | 156 | | |
| 2370.1 | 18 | 73 | −87 | 16/10/12 | 148 | 156 | 165 | |
| 2372.1 | 6 | 326 | −85 | 18/10/12 | 141 | 156 | 166 | |
| 2376.1 | 6 | 264 | 87 | 22/10/12 | 142 | 156 | | |
| 2380.1 | 6 | 289 | 86 | 26/10/12 | 149 | 156 | | |
| 2386.1 | 6 | 345 | −34 | 11/01/12 | 150 | 156 | 166 | |
| 2388.1 | 6 | 326 | 84 | 11/03/12 | 141 | 156 | 165 | |
| 2392.1 | 6 | 342 | 83 | 11/07/12 | 150 | 156 | 156 | |
| 2396.1 | 6 | 14 | 8 | 11/11/12 | 111 | 149 | 156 | 166 |
| 2396.2 | 6 | 357 | 82 | 11/11/12 | 111 | 149 | 156 | 166 |
| 2401.1 | 6 | 29 | 32 | 16/11/12 | 150 | 156 | 165 | |

Thus, the observed agreement between both methods varies between 73 and 95% depending on the layer.

The rotational temperature profiles from the selected dataset are presented in Fig. 8 (left panel). The red dashed profile in the right panel is the mean rotational temperature profile, obtained using a linear sliding average, in which the value for each altitude level is obtained considering the values within a $\pm 5$ km range around this point. The mean hydrostatic temperature profile is presented in all Panels as the black profile. The envelopes and horizontal lines are the $1-\sigma$ uncertainties on the temperature profiles and mean values. The colour code of the profiles is the orbit number: bluish colours for the first ones, reddish colours for the last ones.

In the 90–120 km region, a good statistical match is observed between the rotational and hydrostatic profiles: a systematic overlap of the temperature profiles within their uncertainties is observed. The mean hydrostatic and rotational temperature profiles are in agreement within their respective error bars. The hydrostatic temperature maximum around 105 km is not observed in the rotational temperature profiles, even if temperatures are similar, probably because no rotational temperature measurements are available at lower altitude.

As already mentioned, few measurements are available in the cold layer region (between 120 and 135 km): only one absorption band is strong enough to have a structure above the noise and weak enough not to be saturated. But, this band is overlapped by stronger bands located nearby. These few measurements have large error bars, between 50 and 100 K, and are within the uncertainty on the hydrostatic temperature. We see in the right Panel of Fig. 8 that the 110 K hydrostatic temperature minimum is not clearly reproduced in the rotational temperature profiles, even if the rotational temperature profile remains within the uncertainty of the hydrostatic temperature profile: the scarcity of the measurements and the large error bars on the temperature retrievals at these altitudes limit the validation using this method.

At higher altitude, in the 135–150 km region, a good agreement is obtained between the rotational and hydrostatic profiles. The warm layer at 145 km is well reproduced in the mean rotational temperature profile. Above 150 km, the mean rotational temperature starts to deviate from the hydrostatic temperature profile, even if it remains within its uncertainty. At these altitudes, the hydrostatic temperatures are less frequent. Indeed, a boundary condition on the temperature is needed at the top of each profile, to solve the hydrostatic differential equation. With decreasing altitude, the hydrostatic temperature profiles tend to be independent of the initial condition after one scale height ($\sim$4 km); so, usually below 150 km.

Finally, the mean difference between each rotational temperature profile calculated for a given order of a given spectral bin and the hydrostatic temperature at the same altitude levels has been calculated. This difference is weighted by the uncertainty on the rotational temperature. The results are presented in Fig. 9 for the whole data set. The temperature difference is always smaller than the mean error on the hydrostatic temperature. The mean difference is $-7.8$ K and the standard deviation is equal to 37.6 K.

Comparison between the SOIR hydrostatic temperature profiles and literature temperature profiles is extensively described in the Mahieux et al. (2015) companion paper, where a good agreement is reported.

The analysis presented here indicates that there is – within the measurement accuracy – no evidence for a breakdown of rotational local thermodynamical equilibrium (LTE) at the sounded altitudes of the Venus terminator. More spectra, impeding smaller noise, at the highest altitude range would be needed for a more precise determination of the altitude and magnitude of the rotational LTE breakdown as well as to study vibrational non-LTE in hot bands.

## 5. Conclusions

The temperature retrieval from the SOIR spectra has been performed using the rotational structure recorded in the transmittance spectra. The paper describes the approximations made to simplify the retrieval process, and the sources of uncertainties they introduce. Also, the instrumental effects are carefully described and their influence on the retrieval is addressed. The different sources of error and approximations have been cautiously studied and described, in order to evaluate the error made on the

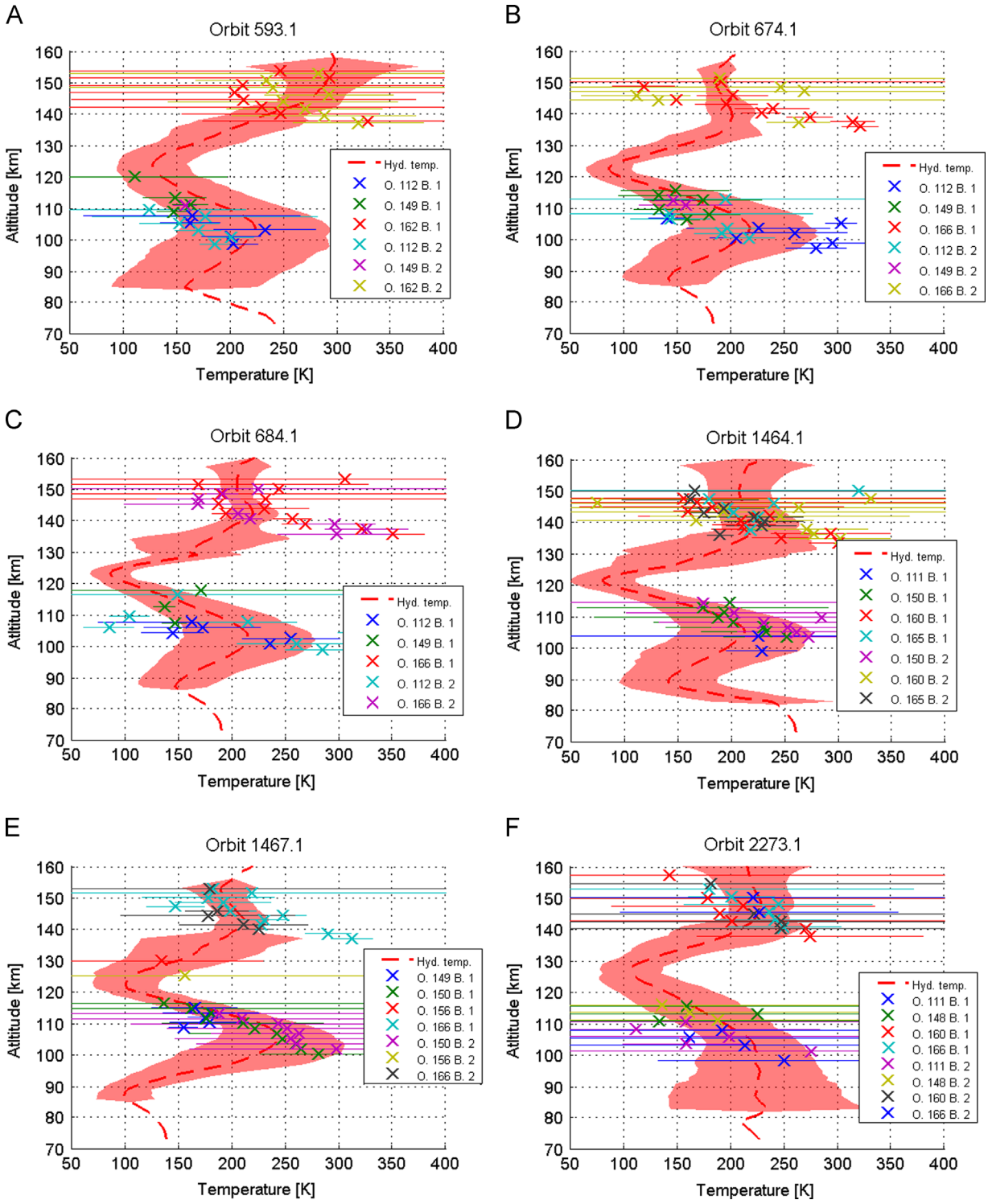


**Fig. 7.** Comparison between the hydrostatic temperature profile (dashed red) and the rotational temperature profiles (coloured crosses) calculated for different orders and bins for six selected orbits: polar region 674.1 (24/02/2008, AM), 684.1 (05/03/2008 AM), 1464.1 (24/04/2010 PM), 1467.1 (27/04/2010 PM), equatorial region 593.1 (05/12/2007 AM) and 2273.1 (11/07/2012 PM). The hydrostatic error is represented by the reddish envelope, and the rotational temperature error bars are the horizontal lines. (For interpretation of the references to color in this figure legend, the reader is referred to the web version of this article.)

simplified temperature retrieval. The noise in the spectra has been found to be the largest source of error ranging from 20 to 200 K.

In the 90 to 100 km region the rotational temperature increases showing mean values from $180 \pm 103$ K ($2-\sigma$ standard deviation) at 92 km to $220 \pm 86$ K at 98 km. At this altitude, an inversion is observed, and the temperature decreases to $151 \pm 69$ K at 116 km. In the 115 to 140 km region, the temperature increases, to a maximum value of $204 \pm 54$ K observed at 140 km. Above, the temperature decreases and is equal to $124 \pm 83$ K at 159 km. A statistical analysis shows that the temperature inversions are well reproduced by both methods.

The rotational temperature measurements corresponding to the cold layer region, previously observed using the hydrostatic temperatures at an altitude of 120–130 km, are scarce. There is

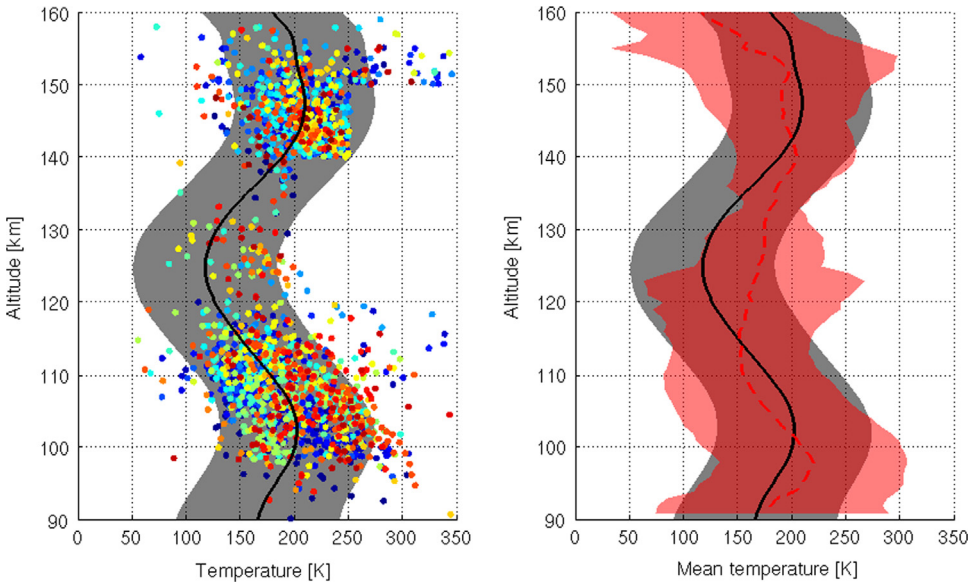


**Fig. 8.** Rotational temperature profiles calculated for the dataset in Table 3 (coloured points). In the left panel, the derived rotational temperatures are shown (the error are not shown for clarity). The colour code is the orbit number: blue for the first orbits, red for the last ones. The black profile and its envelope is the mean hydrostatic profile from all these orbits. In the right panel the mean rotational temperature profile is presented as the red dashed curve, together with its uncertainty (reddish envelope). (For interpretation of the references to color in this figure legend, the reader is referred to the web version of this article.)

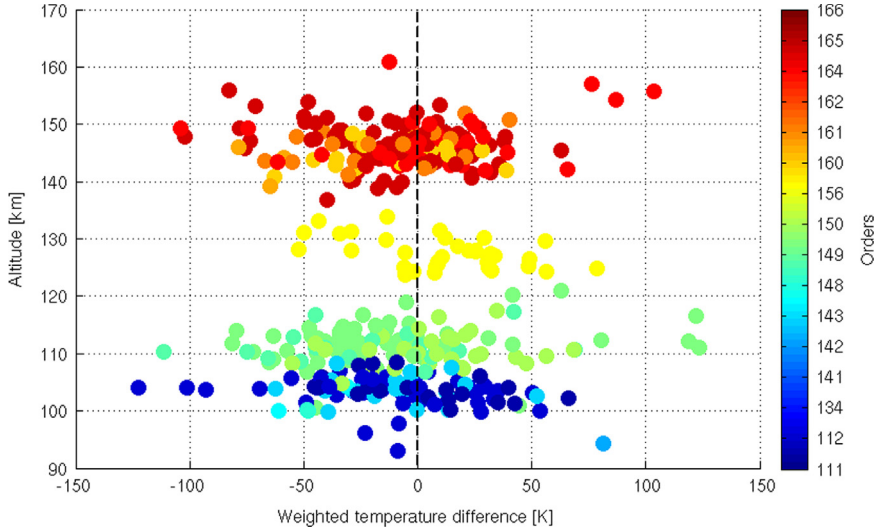


**Fig. 9.** Weighted mean difference between the hydrostatic and rotational temperature profiles for all the retrieved temperature profiles as a function of the altitude. The colour code is the order, defined in the colour bar on the right hand side. The altitude for each point is the mean altitude of the profile. The mean difference is −7.8 K and the standard deviation is 37.6 K. (For interpretation of the references to color in this figure legend, the reader is referred to the web version of this article.)

only one $CO_2$ band for which spectra are usable at these altitudes: the $10^0 1(2)–00^0 0(1)$ of isotopologue $^{13}C^{16}O_2$ measured in order 156. Unfortunately; in these spectra, the superposition of many slightly weaker bands is observed, together with much stronger bands coming from adjacent orders. For these two reasons, even if order 156 was measured many times, few rotational temperature results are available. The temperature obtained from these few available measurements is however within the uncertainty of the hydrostatic temperature at these altitudes.

The present works shows that the derived rotational temperature structure is consistent with that obtained previously which showed a succession of warm and cold layers (Mahieux et al., 2015, 2012). In particular, the consistency is clear in the two warm layers at 95–105 km and in the 140–150 km, although it is more limited in the cold layer in the 110–120 km, where the noise is larger. However the large errors at the cold layer prevent us from making a strong statement on such temperature structure. Other measurements of temperature in the Venus upper atmosphere terminator are thus needed to give further evidence of these cold and warm layers, although model simulations seems also to support that structure (Bougher et al., 2015).

## Acknowledgements

Venus Express is a planetary mission from the European Space Agency (ESA). We wish to thank all ESA members who participated in the mission, in particular, H. Svedhem, D. Titov and O. Witasse. We thank our collaborators at IASB-BIRA (Belgium), Latmos (France), and IKI (Russia). We thank CNES, CNRS, Roskosmos, and the Russian Academy of Science. This research program was supported by the Belgian Federal Science Policy Office and the European Space Agency (ESA, PRODEX program, contracts C 90268, 90113, and 17645). We acknowledge the support of the

"Interuniversity Attraction Poles" programme financed by the Belgian government (Planet TOPERS). This work was partially funded with a *Court séjour* grant of the Belgian *Fonds National de la Recherche Scientifique* and with an *Excellence* grant of *Wallonie-Bruxelles International*. The IAA team was supported by the Spanish MINECO under grant AYA2011-23552, under the CONSOLIDER program CSD2009-00038 and under EC FEDER funds. The author would like to thank the FNRS for the *Chargé de Recherche* position, Jean Vander Auwera from the Université Libre de Bruxelles for his kind help concerning the spectroscopic equations, as well as the reviewers for their useful comments.

## References

Amyay, B., 2012. Etude détaillée et modélisation globale du spectre de vibration-rotation de $^{12}C_2H_2$. Faculté des Sciences-Physique. Univ. Libre de Bruxelles, Belgium (Thesis).

Bertaux, J.L., Nevejans, D., Korablev, O., Villard, E., Quémerais, E., Neefs, E., Montmessin, F., Leblanc, F., Dubois, J.P., Dimarellis, E., Hauchecorne, A., Lefevre, F., Rannou, P., Chaufray, J.Y., Cabane, M., Cernogora, G., Souchon, G., Semelina, F., Reberac, A., Van Ransbeek, E., Berkenbosch, S., Clairquin, R., Muller, C., Forget, F., Hourdin, F., Talagrand, O., Rodin, A., Fedorova, A., Stepanov, A., Vinogradov, A., Kiselev, A., Kalinnikov, Y., Durry, G., Sandel, B., Stern, A., Gérard, J.C., 2007. SPICAV on Venus Express: three spectrometers to study the global structure and composition of the Venus atmosphere. Planet. Space Sci. 55, 1673–1700.

Bougher, S.W., 1995. Comparative thermospheres: Venus and Mars. Adv. Space Res. 15, 21–45.

Bougher, S.W., Brecht, A., Schulte, R., Fischer, J., Parkinson, C., Mahieux, A., Wilquet, V., Vandaele, A.C., 2015. Upper atmosphere temperature structure at the Venusian terminators: a comparison of SOIR and VTGCM results. Planet. Space Sci. 113-114, 337–347.

Brecht, A., Bougher, S.W., 2012. Dayside thermal structure of Venus' upper atmosphere characterized by a global model. J. Geophys. Res. Planets, 117.

Clancy, R.T., Sandor, B.J., Moriarty-Schieven, G., 2003. Observational definition of the Venus mesopause: vertical structure, diurnal variation, and temporal instability. Icarus 161, 1–16.

Clancy, R.T., Sandor, B., Moriarty-Schieven, G., 2012. Thermal structure and CO distribution for the Venus mesosphere/lower thermosphere: 2001–2009 inferior conjunction sub-millimeter CO absorption line observations. Icarus 217, 779–793.

Hedin, A.E., Niemann, H.B., Kasprzak, W.T., 1983. Global empirical model of the Venus thermosphere. J. Geophys. Res. 88, 73–83.

Herzberg, G., 1950. Spectra of Diatomic Molecules, second ed. D. Van Nostrand company, Inc, Princeton.

Johns, J.W.C., Vander Auwera, J., 1990. Absolute intensities in CO*: the v2 fundamental near 15 microns. J. Mol. Spectrosc. 140, 71.

Mahieux, A., 2011. Inversion of the Infrared Spectra Recorded by the SOIR Instrument on Board Venus Express. Univ. Libre de Bruxelles, Belgium (Thesis).

Mahieux, A., Berkenbosch, S., Clairquin, R., Fussen, D., Mateshvili, N., Neefs, E., Nevejans, D., Ristic, B., Vandaele, A.C., Wilquet, V., Belyaev, D., Fedorova, A., Korablev, O., Villard, E., Montmessin, F., Bertaux, J.L., 2008. In-flight performance and calibration of SPICAV/SOIR on-board Venus Express. Appl. Opt. 47, 2252–2265.

Mahieux, A., Vandaele, A.C., Bougher, S.W., Drummond, R., Robert, S., Wilquet, V., Piccialli, A., Montmessin, F., Tellmann, S., Pätzold, M., Häusler, B., Bertaux, J.L., 2015. Update of the Venus density and temperature profiles at high altitude measured by SOIR on board Venus Express. Planet. Space Sci. 113-114, 310–321.

Mahieux, A., Vandaele, A.C., Drummond, R., Robert, S., Wilquet, V., Fedorova, A., Bertaux, J.L., 2010. Densities and temperatures in the Venus mesosphere and lower thermosphere retrieved from SOIR onboard Venus Express: retrieval technique. J. Geophys. Res. 115, http://dx.doi.org/10.1029/2010JE003589.

Mahieux, A., Vandaele, A.C., Robert, S., Wilquet, V., Drummond, R., Montmessin, F., Bertaux, J.L., 2012. Densities and temperatures in the Venus mesosphere and lower thermosphere retrieved from SOIR on board Venus Express: carbon dioxide measurements at the Venus terminator. J. Geophys. Res. 117, http://dx.doi.org/10.1029/2012JE004058.

Mahieux, A., Wilquet, V., Drummond, R., Belyaev, D., Fedorova, A., Vandaele, A.C., 2009. A new method for determining the transfer function of an acousto optical tunable filter. Opt. Express 17, 2005–2014.

Malathy Devi, V.M., Benner, D.C., Rinsland, C.P., Smith, M.A.H., 1998. Absolute rovibrational intensities of $^{12}C^{16}O_2$ absorption bands in the 3090–3850 $cm^{-1}$ spectral region. J. Quant. Spectrosc. Radiat. Transfer 60, 741.

Nevejans, D., Neefs, E., Van Ransbeeck, E., Berkenbosch, S., Clairquin, R., De Vos, L., Moelans, W., Glorieux, S., Baeke, A., Korablev, O., Vinogradov, I., Kalinnikov, Y., Bach, B., Dubois, J.P., Villard, E., 2006. Compact high-resolution space-borne echelle grating spectrometer with *AOTF* based on order sorting for the infrared domain from 2.2 to 4.3 micrometer. Appl. Opt. 45, 5191–5206.

Piccialli, A., Montmessin, F., Belyaev, D., Mahieux, A., Fedorova, A., Marcq, E., Bertaux, J.L., Vandaele, A.C., Korablev, O., 2015. Thermal structure of Venus upper aymosphere measured by stellar occultations with SPICAV/Venus Express. Planet. Space Sci. 113-114, 322–336.

Piccialli, A., Tellmann, S., Titov, D., Limaye, S.S., Khatuntsev, I.V., Pätzold, M., Häusler, B., 2012. Dynamical properties of the Venus mesosphere from the radio-occultation experiment VeRa onboard Venus Express. Icarus 217, 669–681.

Rothman, L.S., Gordon, I.E., Babikov, Y., Barbe, A., Benner, D.C., Bernath, P.F., Bizzocchi, L., Boudon, V., Brown, L.R., Campargue, A., Chance, K.V., Cohen, E.A., Coudert, L.H., Devi, V.M., Drouin, B.J., Fayt, A., Flaud, J.-M., Gamache, R., Harrison, J.J., Hartmann, J.M., Hill, C., Hodges, J., Jacquemart, D., Jolly, A., Lamouroux, J., LeRoy, R.J., Li, G., Long, D.A., Lyulin, O.M., Mackie, C.J., Massie, S., Mikhailenko, S., Muller, H.S.P., Naumenko, O., Nikitin, A., Orphal, J., Perevalov, V., Perrin, A., Polovtseva, E.R., Richard, C., Smith, M.A.H., Starikova, E., Sung, K., Tashkun, S., Tennyson, J., Toon, G., Tyuterev, V.G., Wagner, G., 2013. The HITRAN2012 molecular spectroscopic database. J. Quant. Spectrosc. Radiat. Transfer 130, 4.

Rothman, L.S., Jaquemart, D., Barbe, A., Benner, C., Birk, M., Brown, L.R., Carleer, M., Chackerian Jr., C., Chance, K.V., Coudert, L.H., Dana, V., Devi, M., Flaud, J.-M., Gamache, R.B., Goldman, A., Hartmann, J.-M., Jucks, K.W., Maki, A.G., Mandin, J.-Y., Massie, S.T., Orphal, J., Perrin, A., Rinsland, C.P., Smith, M.A.H., Tennyson, J., Tolchenov, R.N., Toth, R.A., Vander Auwera, J., Varanasi, P., Wagner, G., 2005. The HITRAN 2004 molecular spectroscopic database. J. Quant. Spectrosc. Radiat. Transfer 96, 139–204.

Rothman, L.S., Young, L.D.G., 1981. Infrared energy levels and intensities of carbon dioxide. J. Quant. Spectrosc. Radiat. Transfer 25, 505–524.

Seiff, A., Kirk, D.B., Young, R.E., Blanchard, R.C., Findlay, J.T., Kelly, G.M., Sommer, S.C., 1980. Measurements of thermal structure and thermal contrasts in the atmosphere of Venus and related dynamical observations: results from the four Pioneer Venus probes. J. Geophys. Res. 85, 7903–7933.

Sonnabend, G., Krötz, P., Schmülling, F., Kostiuk, T., Goldstein, J., Sornig, M., Stupar, D., Livengood, T., Hewagama, T., Fast, K., Mahieux, A., 2012. Thermospheric/mesospheric temperatures on Venus: results from ground-based high-resolution spectroscopy of $CO_2$ in 1990/1991 and comparison to results from 2009 and between other techniques. Icarus 217, 856–862.

Titov, D.V., Svedhem, H., Koschny, D., Hoofs, R., Barabash, S., Bertaux, J.L., Drossart, P., Formisano, V., Haüsler, B., Korablev, O., Markiewicz, W., Nevejans, D., Pätzold, M., Piccioni, G., Zhang, T., Merritt, D., Witasse, O., Zender, J., Accomazzo, A., Sweeney, M., Trillard, D., Janvier, M., Clochet, A., 2006a. Venus Express science planning. Planet. Space Sci. 54, 1279–1297.

Titov, D.V., Svedhem, H., McCoy, D., Lebreton, J.P., Barabash, S., Bertaux, J.L., Drossart, P., Formisano, V., Haeusler, B., Korablev, O.I., Markiewicz, W., Neveance, D., Petzold, M., Piccioni, G., Zhang, T.L., Taylor, F.W., Lellouch, E., Koschny, D., Witasse, O., Warhaut, M., Accomazzo, A., Rodrigues-Cannabal, J., Fabrega, J., Schirmann, T., Clochet, A., Coradini, M., 2006b. Venus Express: scientific goals, instrumentation and scenario of the mission. Cosmic Res. 44, 334–348.

Toth, R.A., Miller, C.E., Brown, L.R., Devi, V.M., Benner, C., 2007. Line positions and strengths of $^{16}O^{12}C^{18}O$, $^{18}O^{12}C^{18}O$ and $^{17}O^{12}C^{18}O$ between 2200 and 7000 $cm^{-1}$. J. Mol. Spectrosc. 243, 43–61.

Vandaele, A.C., Mahieux, A., Robert, S., Berkenbosch, S., Clairquin, R., Drummond, R., Letocart, V., Neefs, E., Ristic, B., Wilquet, V., Colomer, F., Belyaev, D., Bertaux, J.L., 2013. Improved calibration of SOIR/Venus Express spectra. Opt. Express 21, 21148.

Zasova, L.V., Moroz, V.I., Linkin, V.M., Khatountsev, I.A., Maiorov, B.S., 2006. Structure of the Venusian atmosphere from surface up to 100 km. Cosmic Res. 44, 364–383.